

Revealing intrinsic domains and fluctuations of moiré magnetism by a wide-field quantum microscope

Mengqi Huang^{1,+}, Zeliang Sun^{2,+}, Gerald Yan¹, Hongchao Xie², Nishkarsh Agarwal³, Gaihua Ye⁴, Suk Hyun Sung³, Hanyi Lu¹, Jingcheng Zhou¹, Shaohua Yan⁵, Shangjie Tian^{5,6}, Hechang Lei⁵, Robert Hovden³, Rui He⁴, Hailong Wang⁷, Liuyan Zhao^{2,*}, and Chunhui Rita Du^{1,7,*}

¹Department of Physics, University of California, San Diego, La Jolla, California 92093, USA

²Department of Physics, the University of Michigan, Ann Arbor, Michigan 48109, USA

³Department of Materials Science and Engineering, University of Michigan, Ann Arbor, Michigan 48109, USA

⁴Department of Electrical and Computer Engineering, Texas Tech University, Lubbock, Texas 79409, USA

⁵Laboratory for Neutron Scattering, and Beijing Key Laboratory of Optoelectronic Functional Materials MicroNano Devices, Department of Physics, Renmin University of China, Beijing 100872, China

⁶School of Materials Science and Engineering, Anhui University, Hefei 230601, China

⁷Center for Memory and Recording Research, University of California, San Diego, La Jolla, California 92093

*Corresponding authors: lyzhao@umich.edu; cldu@physics.ucsd.edu

+These authors contributed equally

Abstract: Moiré magnetism featured by stacking engineered atomic registry and lattice interactions has recently emerged as an appealing quantum state of matter at the forefront condensed matter physics research. Nanoscale imaging of moiré magnets is highly desirable and serves as a prerequisite to investigate a broad range of intriguing physics underlying the interplay between topology, electronic correlations, and unconventional nanomagnetism. Here we report spin defect-based wide-field imaging of magnetic domains and spin fluctuations in twisted double trilayer (tDT) chromium triiodide CrI₃. We explicitly show that intrinsic moiré domains of opposite magnetizations appear over arrays of moiré supercells in low-twist-angle tDT CrI₃. In contrast, spin fluctuations measured in tDT CrI₃ manifest little spatial variations on the same mesoscopic length scale due to the dominant driving force of intralayer exchange interaction. Our results enrich the current understanding of exotic magnetic phases sustained by moiré magnetism and highlight the opportunities provided by quantum spin sensors in probing microscopic spin related phenomena on two-dimensional flatland.

Moiré magnetism, an emergent class of quantum states of matter, features periodically modulated magnetic order and interaction, and provides an appealing platform for exploring emergent spin transport and dynamic behaviors in solid states¹⁻¹⁰. Very recently, the microscopic spin arrangement within individual magnetic moiré supercells has been directly visualized in twisted double trilayer (tDT) chromium triiodide CrI₃². Same as all spontaneous symmetry breaking phases, degenerate domain states of moiré magnetism are anticipated and should manifest on length scales across multiple moiré wavelengths. However, there have been few studies on the intrinsic domain phases and structures of moiré magnetic orders. Here we report nitrogen-vacancy (NV) center-based¹¹⁻¹³ wide-field imaging of magnetic domains and spin fluctuations in tDT CrI₃. We show that intrinsic moiré domains of opposite magnetizations appear on a mesoscopic length scale in low-twist-angle (0.3°) tDT CrI₃, and that the formed domain states can be trained by applying a small external magnetic field. In contrast, such mesoscopic domain features are absent in large-twist-angle (15°) tDT and pristine CrI₃. Our work adds a further ingredient for the burgeoning topic of moiré magnetism, highlighting the significant potential of quantum metrology in studying unconventional nanomagnetism hosted by exotic condensed matter systems.

Moiré superlattices consisting of atomically thin van der Waals crystals have attracted tremendous attention on the forefront of quantum materials research study^{14,15}. By stacking layers of two-dimensional (2D) materials with a small twist angle or a lattice mismatch, a plethora of exotic electronic, photonic, and magnetic phases can be created and engineered due to the introduction of a periodically modulated atomic registry on the scale of the moiré wavelengths. Notable examples include flat band-based correlated and topological electronic states^{14,15}, moiré magnetism¹⁻¹⁰, and moiré excitons¹⁶⁻¹⁹. Over the past few years, 2D materials such as graphene^{14,15,20,21}, transition metal dichalcogenides^{16,18,19,22}, and van der Waals magnets¹⁻⁵ have been under intensive investigations in this context, and transformative quantum technologies built on moiré materials are underway.

In contrast to the study of the charge degree of freedom which has achieved a remarkable success in controlling the electronic and excitonic properties of moiré superlattices^{14,15}, the magnetic counterpart, moiré magnetism, remains relatively underexplored. An apparent challenge results from the limited experimental tools capable of resolving spatially varying magnetic patterns hosted by moiré materials at the nanoscale. While the noncollinear spin textures^{5,10}, topological skyrmion lattices^{6,7}, stacking dependent magnetism⁸ and magnon bands⁹ have been theoretically predicted in van der Waals magnet-based moiré superlattices, real space imaging of these emergent magnetic features remains as a formidable challenge at the current state of the art. Here we explore NV centers¹¹⁻¹³, optically active atomic defects in diamond, to perform wide-field magnetometry imaging²³⁻²⁶ of twisted CrI₃. Taking advantage of the appreciable field sensitivity and spatial resolution of NV centers, we have observed stacking-induced intrinsic (ferro)magnetic domains spontaneously formed over arrays of moiré supercells in low-twist-angle tDT CrI₃. Furthermore, we reveal a uniform spatial distribution of spin fluctuations in tDT CrI₃ despite the presence of magnetic domains, suggesting that spin fluctuations in moiré magnets are mainly driven by the intralayer exchange interaction instead of the spatially modulated interlayer coupling.

Before discussing the details of our experimental results, we first present the device structures and our measurement platform as illustrated in Fig. 1a. In this work, we fabricated tDT CrI₃ devices by the standard “tear-and-stack” technique and encapsulated them with hexagonal boron nitride flakes^{1-3,20,27}. Figure 1b shows a prepared tDT CrI₃ sample (top) made from an atomically thin CrI₃ flake (bottom). The twist angle was controlled to be ~0.3° in order to obtain a relatively large moiré period of ~130 nm (see Supplementary Information Note 1 for details). The

prepared device was released onto a diamond membrane for NV wide-field magnetometry measurements. NV centers at the diamond surface are created by $^{14}\text{N}^+$ ion implantation with an energy of 3 keV, and the depth of implanted NVs is estimated to be $\sim 10\text{ nm}^{28}$. In the current study, we utilize NV ensembles to perform nanoscale imaging of the static magnetic textures and dynamic spin fluctuations in the prepared tDT CrI_3 devices. Magnetic circular dichroism (MCD) measurements⁵ on control samples are used to qualitatively diagnose the magnetic properties of twisted and pristine CrI_3 .

Pristine CrI_3 belongs to the A-type antiferromagnet family showing the characteristic even-odd layer-number determined (un)compensated magnetization in the magnetic ground state^{29,30}. For twisted CrI_3 , the magnetic moment is spatially modulated within a moiré unit cell depending on the local atomic registry¹⁻³. The magnitude and sign of the interlayer exchange coupling varies from the monoclinic (AB') to rhombohedral (AB) stacking geometries leading to co-existing ferromagnetic and antiferromagnetic order in tDT CrI_3 , as illustrated in Fig. 1a. Such stacking induced spin arrangement within individual moiré supercells has been visualized by scanning NV magnetometry in a previous work². The current study mainly focuses on real-space imaging of the energetically degenerate domain states, with opposite magnetizations and related by the time-reversal operation, formed over arrays of moiré supercells in tDT CrI_3 . Such domain states should extend over multiple moiré periods at a mesoscopic length scale as shown in Fig. 1c, and their degeneracy is controllable by external stimuli such as magnetic field, thermal cycles, and local defects. The prominent spatial magnetic “inhomogeneity” together with reduced inter-domain coupling naturally results in spontaneous formation of stacking-induced (ferro)magnetic domains in tDT CrI_3 . A major goal of the present work is to utilize NV centers, a sensitive probe to local stray fields, to identify the real-space distribution of these novel magnetic domain states.

We first use MCD to qualitatively reveal the magnetic properties of pristine and twisted CrI_3 samples. The MCD measurement is sensitive to the total magnetization perpendicular to the sample surface, serving as an ideal experimental probe for investigating the magnetic ground state of CrI_3 with out-of-plane anisotropy^{1,3,5}. Our MCD measurements were performed at a temperature of 12 K with an out-of-plane magnetic field, and the measured magneto-optical signals were averaged over a micrometer-sized laser spot on the sample surface. Figures 2a–2c show field dependent MCD signals of pristine trilayer, 0.3° tDT, and six-layer CrI_3 samples, respectively. The trilayer CrI_3 with uncompensated magnetization in the ground state exhibits a characteristic hysteresis loop centered at zero magnetic field and spin-flip transitions at $\pm 1.6\text{ T}$. And the six-layer CrI_3 sample with fully compensated magnetization shows vanishingly small MCD signals at zero magnetic field and two field-driven magnetic phase transitions at $\pm 0.7\text{ T}$ and $\pm 1.6\text{ T}$. Notably, 0.3° tDT CrI_3 exhibits a mixture of the magnetic phases of the trilayer and six-layer samples, suggesting co-existence of ferromagnetic and antiferromagnetic order due to the spatially modulated stacking geometries.

Next, we present NV wide-field magnetometry²³⁻²⁶ results to image the real space magnetic patterns of the CrI_3 devices. Wide-field magnetometry exploits the Zeeman effect¹² of NV ensembles to measure local magnetic stray fields emanating from the CrI_3 devices (see Supplementary Information Note 2 for details). Figures 2d and 2e show 2D magnetic stray field maps of pristine trilayer and six-layer CrI_3 samples measured at a temperature $T = 5\text{ K}$ with an out-of-plane magnetic field $B_{\text{ext}} = 71\text{ G}$. The trilayer CrI_3 sample exhibits a robust stray field B_s arising from the uncompensated magnetic moment while the six-layer one shows a vanishingly small stray field as expected due to its antiferromagnetic ground state. In contrast with the nearly uniform stray field distribution in the pristine samples, the tDT CrI_3 device, after field cooling with a

positive field of ~ 71 G, shows distinct multidomain features with stray fields of opposite polarity emanating from individual domains (Fig. 2f). When reversing the sign of the external magnetic cooling field, the polarity of the individual domains also changes (Fig. 2g), indicating that the stacking-induced magnetic degeneracy can be controlled by the thermal cycle and field history. Through well-established reverse-propagation protocols, the corresponding magnetization maps of the tDT CrI₃ sample can be reconstructed (Figs. 2h–2i, see Supplementary Information Note 3 for details). One can see that the tDT CrI₃ sample consists of magnetic domains of opposite magnetizations ($\sim \pm 15 \mu\text{B}/\text{nm}^2$). The nonvanishing magnetic moment results from the one layer of uncompensated magnetization for each individual CrI₃ trilayer as illustrated in Fig. 1a. It is worth mentioning that the measured magnetization reflects a spatial average over the ferromagnetic and antiferromagnetic regions within moiré supercells, from which the fraction of rhombohedral order is estimated to be 60% in 0.3° tDT CrI₃. The lateral dimensions of the observed magnetic domains in tDT CrI₃ lies on the micrometer length scale, which is orders of magnitude larger than the estimated moiré wavelength. The opposite signs of the measured static magnetizations in combination with the mesoscopic characteristic length scale suggest that the observed magnetic patterns result from intrinsic (ferro)magnetic domains consisting of multiple moiré supercells in tDT CrI₃ (see Supplementary Information Note 4 for details). The spatial distribution of the extended magnetic domains in tDT CrI₃ is co-determined by the intrinsic material properties including competition between dipole and exchange interactions, magnetic anisotropy, local defects, strain, as well as the external experimental stimuli. It is instructive to note that such multidomain features disappear in tDT CrI₃ devices with a large twist angle (15°), where pure ferromagnetic order emerges uniformly, showing a clear single magnetic domain (see Supplementary Information Note 5 for details).

We now present systematic NV wide-field magnetometry results to reveal the magnetic phase transition of the tDT CrI₃ sample across the Curie temperature. Figures 3a–3g show the magnetic stray field maps of the prepared 0.3° tDT CrI₃ device measured at temperatures varying from 10 K to 57 K with an external magnetic field B_{ext} of 71 G. In general, the magnetic stray field emanating from the tDT CrI₃ sample decreases with increasing temperature due to reduced static magnetization. In the low temperature regime ($T \leq 36$ K), tDT CrI₃ exhibits robust magnetization owing to the suppressed thermal fluctuations as shown in Figs. 3a–3c. When approaching the magnetic phase transition temperature, the magnetization dramatically decays accompanied by a blurring of the magnetic domain boundaries in tDT CrI₃ (Fig. 3d–3f). Above the Curie temperature, the magnetization distribution pattern gradually disappears over the entire device area (Fig. 3g). Figure 3h summarizes temperature dependent evolution of the magnetic stray field B_s measured at two local domain sites with opposite polarities. The emanating magnetic field exhibits a gradual decay in the low temperature regime ($T < 30$ K), followed by a dramatic drop during the magnetic phase transition of tDT CrI₃ (see Supplementary Information Note 3 for details).

In addition to the d.c. magnetometry measurements presented above, NV centers, known as spin qubits with excellent quantum coherence, provide additional opportunities for probing noncoherent fluctuating magnetic fields that are challenging to access by the conventional magnetometry methods^{31–36}. Next, we apply NV spin relaxometry techniques to spatially image magnetic fluctuations in the prepared tDT CrI₃ device. Thermally induced spin fluctuations in a magnetic sample couple to proximal NV centers through the dipole-dipole interaction. Fluctuating magnetic fields at the NV electron spin resonance (ESR) frequencies accelerate NV spin transitions from the $m_s = 0$ to $m_s = \pm 1$ states, leading to enhancement of the NV spin relaxation rates^{26,34,35,37}.

By measuring the spin-dependent NV photoluminescence, the occupation probabilities of NV spin states can be quantitatively obtained, allowing for extraction of the NV spin relaxation rate which is proportional to the magnitude of the local fluctuating magnetic field transverse to the NV axis^{37,38} (see Supplementary Information Note 6 for details).

Figures 4a–4g present a series of NV spin relaxation rate maps of the 0.3° tDT CrI₃ device measured in a broad temperature range. The background of intrinsic NV spin relaxation has been subtracted to highlight the contribution from the magnetic sample. In the current study, the minimum magnon energy of CrI₃ is larger than the NV ESR frequencies under our experimental conditions. Thus, the measured NV spin relaxation is mainly driven by the longitudinal spin fluctuations of CrI₃, which are further related to the static longitudinal magnetic susceptibility and the diffusive spin transport constant^{26,38}. In the low-temperature regime ($T < 40$ K), magnetic fluctuations in CrI₃ are largely suppressed due to the vanishingly small spin susceptibility, resulting in reduced NV spin relaxation rate (Figs. 4a and 4b). As the temperature increases, the measured NV spin relaxation rate significantly increases near the magnetic phase transition of tDT CrI₃ and reaches the maximum value around the critical point (Figs. 4c–4e), which is attributed to the dramatic enhancement of spin susceptibility of tDT CrI₃ around the Curie temperature. When temperature is above the magnetic phase transition point, spin fluctuations remain active in tDT CrI₃ due to the finite spin-spin correlation in the paramagnetic state^{26,39} (Figs. 4f–4g). Figure 4h summarizes the temperature dependence of the measured NV spin relaxation rate Γ_M with a peak value of 18 kHz around the Curie temperature.

Interestingly, the measured spin fluctuations exhibit a largely uniform spatial distribution over the tDT CrI₃ sample area, in sharp contrast with the static magnetic stray field patterns showing the distinct multidomain features. The magnitude of the spin fluctuations is fundamentally correlated with the spin diffusion constant D and longitudinal magnetic susceptibility χ_0 governed by the exchange energy of magnetic lattices. While the stacking geometries spatially modulate the interlayer coupling strength of the tDT CrI₃ sample, the dominant intralayer exchange interaction largely remains the same. The minimal spatial variation of the measured NV spin relaxation rate indicates that spin fluctuations in tDT CrI₃ are mainly driven by the intralayer exchange interaction while the role of the interlayer coupling is secondary. Invoking a theoretical model developed in Ref. 26, the longitudinal magnetic susceptibility χ_0 and spin diffusion constant D of the tDT CrI₃ sample is extracted to be $(4.0 \pm 0.2) \times 10^{-2} \text{ emu}\cdot\text{cm}^{-3}\cdot\text{Oe}^{-1}$ and $(4.2 \pm 0.3) \times 10^{-5} \text{ m}^2/\text{s}$ at 40 K from the NV relaxometry results (see Supplementary Information Note 7 for details). The spin diffusion constant D reflects the intrinsic spin transport capability of a magnetic system, which is further related to other important material parameters such as spin decay (diffusion) length³⁸. D is fundamentally determined by the magnon velocity v and the momentum relaxation time τ as follows: $D = \frac{v^2\tau}{2}$ ²⁶. Using the obtained spin diffusion constant value, the magnon velocity v in tDT CrI₃ is estimated to be ~ 4.3 km/s when taking a momentum scattering time $\tau \sim 5$ ps, which is in qualitative agreement with the theoretical estimation^{7,40}. The extracted longitudinal magnetic susceptibility χ_0 describes dynamic magnetic responses along the magnetic order direction of tDT CrI₃. It is typically anticipated that χ_0 shows a divergent behavior across the second order phase transition. A detailed knowledge of this material parameter of atomically thin van der Waals magnets, as demonstrated in the current study, will provide an alternative way to investigate the

local magnetic phase variations of emergent material systems on 2D flatland. Building on the current study, we further share the optimism that it would be very interesting to explore the relative contributions of interlayer and intralayer exchange coupling driven spin fluctuations in twisted CrI₃ with different layer thicknesses. Meanwhile, local variations of spin fluctuations may also emerge within individual moiré supercells between the magnetized rhombohedral stacking and zero magnetization monoclinic stacking sites. Here we reserve these exciting experiments for a future study where more advanced NV microscopy techniques with enhanced spatial resolution may be used.

In summary, we have demonstrated NV wide-field imaging of the magnetic domains formed at a mesoscopic length scale of multiple moiré periods in tDT CrI₃. By using NV spin relaxometry techniques, we further probe the spin fluctuations in twisted CrI₃, whose magnitude reaches a maximum around the magnetic phase transition point. In contrast with the static magnetic stray field patterns showing distinct multidomain features, spin fluctuations driven by the intralayer exchange interaction exhibits a largely uniform spatial distribution in tDT CrI₃. We note that multiple tDT CrI₃ samples have been evaluated to ensure the consistency of the presented results (see Supplementary Information Note 8 for details). Our work highlights the significant potential of NV centers for investigating the local static and dynamic magnetic behaviors in emergent moiré superlattices, suggesting new opportunities for probing the interplay between “inhomogeneous” magnetic order, spin transport and dynamic behaviors in a broad range of quantum states of matter.

Acknowledgements. Authors thank Raymond Zhu for insightful discussions. M. H., H. L., H. W., and C. R. D. were supported by the Air Force Office of Scientific Research under award No. FA9550-20-1-0319 and its Young Investigator Program under award No. FA9550-21-1-0125. G. Q. Y., J. Z., and C. R. D. acknowledged the support from U. S. National Science Foundation (NSF) under award No. DMR-2046227 and ECCS-2029558. L. Z. acknowledges support by NSF CAREER grant no. DMR-174774, AFOSR YIP grant no. FA9550-21-1-0065, and Alfred P. Sloan Foundation. R. H. acknowledges support by NSF grant no. DMR-2104036. R. Hovden acknowledges support from the US Army Research Office (W911NF-22-1-0056). H. C. L was supported by the National Key R&D Program of China (Grant No. 2018YFE0202600, 2022YFA1403800), the Beijing Natural Science Foundation (Grant No. Z200005), and the National Natural Science Foundation of China (12274459).

References:

1. Xu, Y. *et al.* Coexisting ferromagnetic–antiferromagnetic state in twisted bilayer CrI₃. *Nat. Nanotechnol.* **17**, 143–147 (2022).
2. Song, T. *et al.* Direct visualization of magnetic domains and moiré magnetism in twisted 2D magnets. *Science* **374**, 1140–1144 (2021).
3. Xie, H. *et al.* Twist engineering of the two-dimensional magnetism in double bilayer chromium triiodide homostructures. *Nat. Phys.* **18**, 30–36 (2022).
4. Cheng, G. *et al.* Electrically tunable moiré magnetism in twisted double bilayers of chromium triiodide. *Nat. Electron.* **6**, 434–442 (2023).
5. Xie, H. *et al.* Evidence of non-collinear spin texture in magnetic moiré superlattices. *Nat. Phys.*, (2023). <https://doi.org/10.1038/s41567-023-02061-z>
6. Tong, Q., Liu, F., Xiao, J. & Yao, W. Skyrmions in the moiré of van der Waals 2D magnets. *Nano Lett.* **18**, 7194–7199 (2018).
7. Akram, M. *et al.* Moiré skyrmions and chiral magnetic phases in twisted CrX₃ (X = I, Br, and Cl) bilayers. *Nano Lett.* **21**, 6633–6639 (2021).
8. Sivadas, N., Okamoto, S., Xu, X., Fennie, Craig. J. & Xiao, D. Stacking-dependent magnetism in bilayer CrI₃. *Nano Lett.* **18**, 7658–7664 (2018).
9. Wang, C., Gao, Y., Lv, H., Xu, X. & Xiao, D. Stacking domain wall magnons in twisted van der Waals magnets. *Phys. Rev. Lett.* **125**, 247201 (2020).
10. Hejazi, K., Luo, Z.-X. & Balents, L. Noncollinear phases in moiré magnets. *Proc. Natl. Acad. Sci.* **117**, 10721–10726 (2020).
11. Degen, C. L., Reinhard, F. & Cappellaro, P. Quantum sensing. *Rev. Mod. Phys.* **89**, 035002 (2017).
12. Rondin, L. *et al.* Magnetometry with nitrogen-vacancy defects in diamond. *Rep. Prog. Phys.* **77**, 056503 (2014).
13. Doherty, M. W. *et al.* The nitrogen-vacancy colour centre in diamond. *Phys. Rep.* **528**, 1–45 (2013).
14. Andrei, E. Y. *et al.* The marvels of moiré materials. *Nat. Rev. Mater.* **6**, 201–206 (2021).
15. Kennes, D. M. *et al.* Moiré heterostructures as a condensed-matter quantum simulator. *Nat. Phys.* **17**, 155–163 (2021).
16. Tran, K. *et al.* Evidence for moiré excitons in van der Waals heterostructures. *Nature* **567**, 71–75 (2019).
17. Huang, D., Choi, J., Shih, C.-K. & Li, X. Excitons in semiconductor moiré superlattices. *Nat. Nanotechnol.* **17**, 227–238 (2022).
18. Jin, C. *et al.* Observation of moiré excitons in WSe₂/WS₂ heterostructure superlattices. *Nature* **567**, 76–80 (2019).
19. Seyler, K. L. *et al.* Signatures of moiré-trapped valley excitons in MoSe₂/WSe₂ heterobilayers. *Nature* **567**, 66–70 (2019).
20. Cao, Y. *et al.* Unconventional superconductivity in magic-angle graphene superlattices. *Nature* **556**, 43–50 (2018).
21. Cao, Y. *et al.* Correlated insulator behaviour at half-filling in magic-angle graphene superlattices. *Nature* **556**, 80–84 (2018).
22. Li, T. *et al.* Quantum anomalous Hall effect from intertwined moiré bands. *Nature* **600**, 641–646 (2021).
23. Lenz, T. *et al.* Imaging topological spin structures using light-polarization and magnetic microscopy. *Phys. Rev. Appl.* **15**, 024040 (2021).

24. Tetienne, J.-P. *et al.* Quantum imaging of current flow in graphene. *Sci. Adv.* **3**, e1602429 (2017).
25. Ku, M. J. H. *et al.* Imaging viscous flow of the Dirac fluid in graphene. *Nature* **583**, 537–541 (2020).
26. McLaughlin, N. J. *et al.* Quantum imaging of magnetic phase transitions and spin fluctuations in intrinsic magnetic topological nanoflakes. *Nano Lett.* **22**, 5810–5817 (2022).
27. Kim, K. *et al.* van der Waals heterostructures with high accuracy rotational alignment. *Nano Lett.* **16**, 1989–1995 (2016).
28. Pham, L. M. *et al.* NMR technique for determining the depth of shallow nitrogen-vacancy centers in diamond. *Phys. Rev. B* **93**, 045425 (2016).
29. Huang, B. *et al.* Layer-dependent ferromagnetism in a van der Waals crystal down to the monolayer limit. *Nature* **546**, 270–273 (2017).
30. Thiel, L. *et al.* Probing magnetism in 2D materials at the nanoscale with single-spin microscopy. *Science* **364**, 973–976 (2019).
31. Andersen, T. I. *et al.* Electron-phonon instability in graphene revealed by global and local noise probes. *Science* **364**, 154–157 (2019).
32. Kolkowitz, S. *et al.* Probing Johnson noise and ballistic transport in normal metals with a single-spin qubit. *Science* **347**, 1129–1132 (2015).
33. McCullian, B. A. *et al.* Broadband multi-magnon relaxometry using a quantum spin sensor for high frequency ferromagnetic dynamics sensing. *Nat. Commun.* **11**, 5229 (2020).
34. Finco, A. *et al.* Imaging non-collinear antiferromagnetic textures via single spin relaxometry. *Nat. Commun.* **12**, 767 (2021).
35. Du, C. *et al.* Control and local measurement of the spin chemical potential in a magnetic insulator. *Science* **357**, 195–198 (2017).
36. Ariyaratne, A., Bluvstein, D., Myers, B. A. & Jayich, A. C. B. Nanoscale electrical conductivity imaging using a nitrogen-vacancy center in diamond. *Nat. Commun.* **9**, 2406 (2018).
37. van der Sar, T., Casola, F., Walsworth, R. & Yacoby, A. Nanometre-scale probing of spin waves using single electron spins. *Nat. Commun.* **6**, 7886 (2015).
38. Flebus, B. & Tserkovnyak, Y. Quantum-impurity relaxometry of magnetization dynamics. *Phys. Rev. Lett.* **121**, 187204 (2018).
39. Huang, M. *et al.* Wide field imaging of van der Waals ferromagnet Fe₃GeTe₂ by spin defects in hexagonal boron nitride. *Nat. Commun.* **13**, 5369 (2022).
40. Chatterjee, S., Rodriguez-Nieva, J. F. & Demler, E. Diagnosing phases of magnetic insulators via noise magnetometry with spin qubits. *Phys. Rev. B* **99**, 104425 (2019).

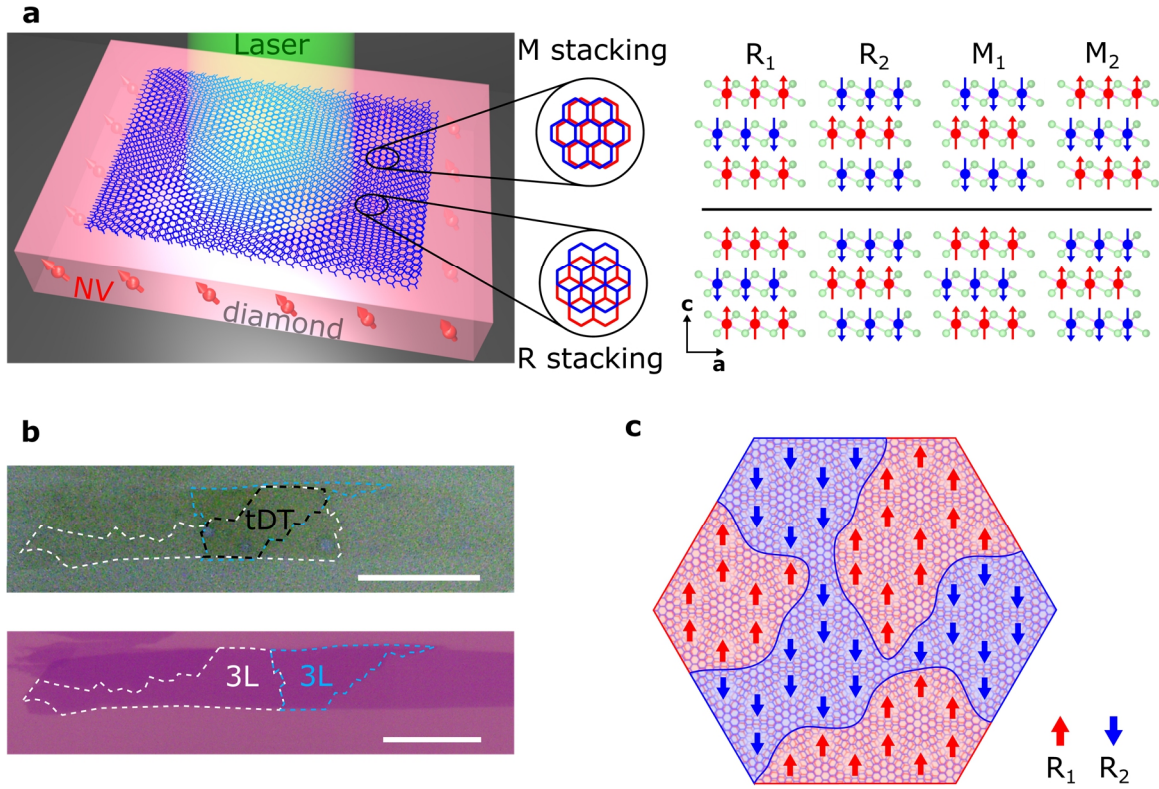


Figure 1. Device structure and NV measurement platform. **a** Left: Schematic illustration of NV wide-field magnetometry measurements of twisted CrI_3 . Right: Monoclinic (AB') and rhombohedral (AB) stacking-induced two-fold degenerate antiferromagnetic (M_1 and M_2) and ferromagnetic (R_1 and R_2) phases in the ground state of tDT CrI_3 . The red and blue arrows represent local magnetization carried by Cr atoms (red and blue balls) at individual layers. The light green balls represent the I atoms. **b** Optical microscopy image of a tDT CrI_3 sample on a diamond membrane (top) prepared from a large-sized trilayer CrI_3 flake on a Si/SiO_2 substrate (bottom) by the “tear and stack” technique. The twisted area is outlined by the black dashed lines, and the original trilayer CrI_3 flake and the tearing boundary is marked with the white and blue dashed lines. Scale bar is $20\ \mu\text{m}$. **c** Schematic of the twisted interface of tDT CrI_3 with a low twist angle. Rhombohedral (AB) stacking-induced ferromagnetic order shows R_1 (red) and R_2 (blue) domains with opposite polarity on an extended length scale that is larger than the moiré period. The red and blue arrows denoting the spin-up and spin-down along the out-of-plane directions, respectively, are used to illustrate the ferromagnetic order at local rhombohedral stacking sites.

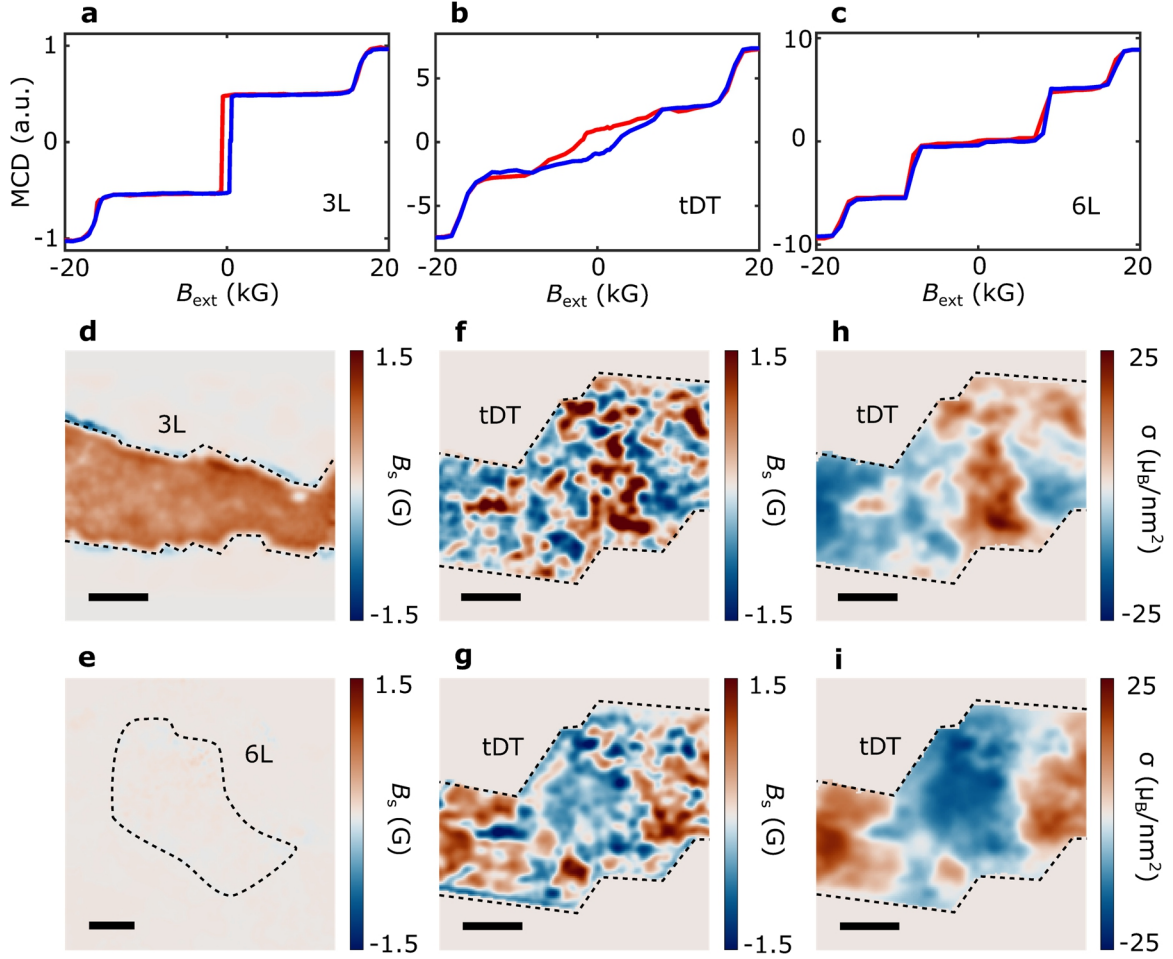


Figure 2. MCD and NV wide-field measurements of CrI_3 samples. **a-c** MCD signals as a function of an out-of-plane magnetic field for trilayer, 0.3° tDT, and six-layer CrI_3 samples. The blue and red curves correspond to increasing and decreasing magnetic field, respectively. **d, e** NV wide-field imaging of magnetic stray fields emanating from pristine trilayer (**d**) and six-layer (**e**) CrI_3 samples. **f, g** Magnetic stray field patterns measured for the 0.3° tDT CrI_3 sample with a positive (**f**) and negative (**g**) cooling field. **h, i** Reconstructed magnetization maps of the tDT CrI_3 sample measured with a positive (**h**) and negative (**i**) cooling field. The black dashed lines outline the boundary of the CrI_3 samples of interest, and the scale bar is $3 \mu\text{m}$ for all the images.

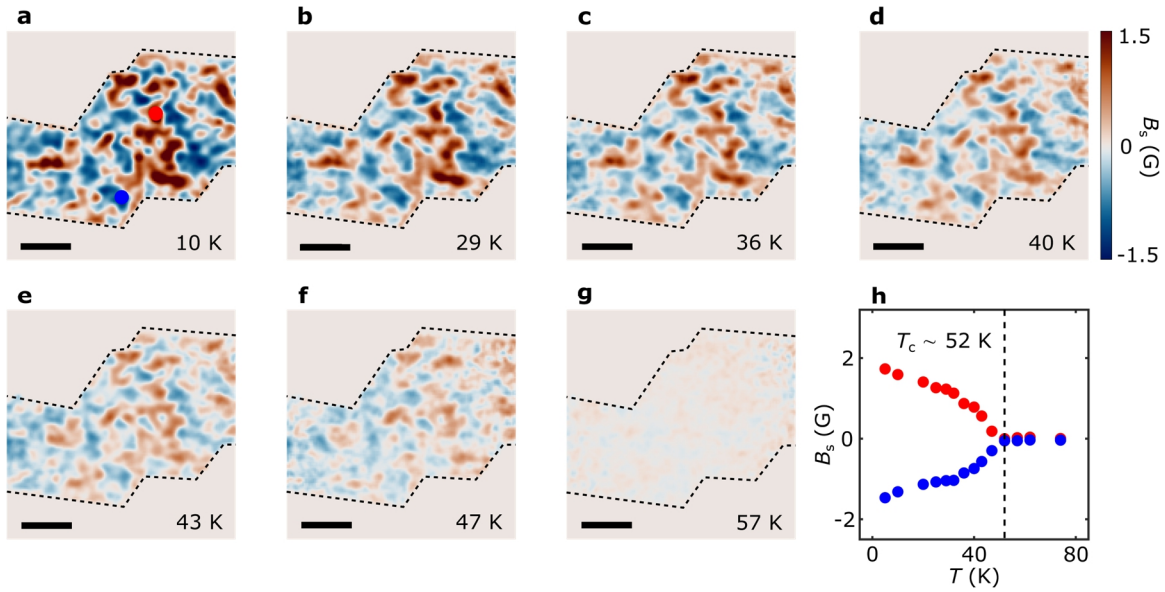


Figure 3. Temperature dependence of twisted magnetism. a-g Stray field patterns of the 0.3° tDT CrI₃ sample measured at an out-of-plane field $B_{\text{ext}} = 71$ G and temperatures of 10 K (a), 29 K (b), 36 K (c), 40 K (d), 43 K (e), 47 K (f), and 57 K (g), respectively. The black dashed lines outline the boundary of the 0.3° tDT CrI₃, and the scale bar is 3 μm. **h** Temperature dependence of the emanating stray field measured at two local magnetic domain sites with opposite polarity, from which the Curie temperature of the 0.3° tDT CrI₃ is estimated to be 52 K (black dashed lines).

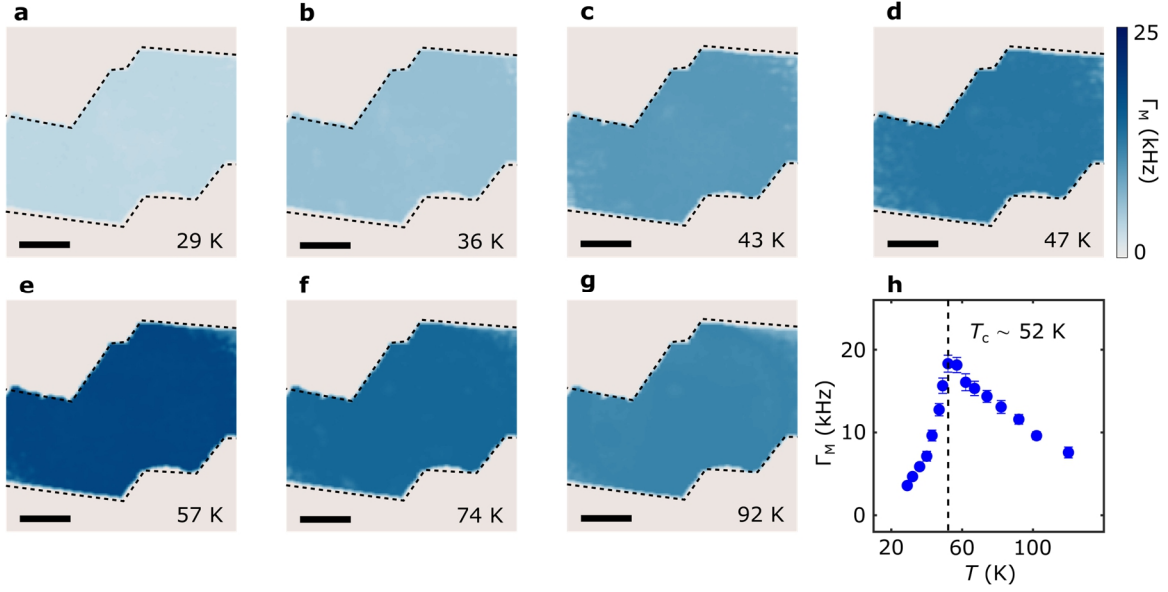


Figure 4. Temperature dependence of spin fluctuations in twisted CrI₃. a-g NV spin relaxation maps for the 0.3° tDT CrI₃ sample measured at temperatures of 29 K (a), 36 K (b), 43 K (c), 47 K (d), 57 K (e), 74 K (f), and 92 K (g), respectively. The NV ESR frequency is set to be 2.78 GHz in these measurements with an external out-of-plane magnetic field $B_{\text{ext}} = 71$ G. The black dashed lines outline the boundary of the tDT CrI₃ sample, and the scale bar is 3 μm. h Temperature dependence of NV spin relaxation rate Γ_M measured at NV centers underneath the tDT CrI₃ device. The dashed lines mark the estimated Curie temperature of tDT CrI₃.